



Aberration measurement of the probe-forming system of an electron microscope using two-dimensional materials



Hidetaka Sawada^{a,b,c,d,*}, Christopher S. Allen^{a,b}, Shanshan Wang^b, Jamie H. Warner^b, Angus I. Kirkland^{a,b}

^a Electron Physical Sciences Imaging Centre (ePSIC), Diamond Light Source Ltd, Didcot, Oxford OX11 0DE, UK

^b Department of Materials, University of Oxford, Parks Road, Oxford OX1 3PH, UK

^c JEOL UK Ltd., Silver Court Watchmead Welwyn Garden City, Herts AL7 1LT, UK

^d Research acceleration program, Japan Science and Technology Agency, K's Gobancho, 7, Gobancho, Chiyoda-ku, Tokyo 102-0076, Japan

ARTICLE INFO

Article history:

Received 13 February 2017

Revised 27 May 2017

Accepted 19 June 2017

Available online 5 July 2017

Keywords:

Geometric aberration

Chromatic aberration

STEM

Ronchigram

Aberration corrector

ABSTRACT

The geometric and chromatic aberration coefficients of the probe-forming system in an aberration corrected transmission electron microscope have been measured using a Ronchigram recorded from monolayer graphene. The geometric deformations within individual local angular sub-regions of the Ronchigram were analysed using an auto-correlation function and the aberration coefficients for the probe forming lens were calculated. This approach only requires the acquisition of a single Ronchigram allowing rapid measurement of the aberration coefficients. Moreover, the measurement precision for defocus and two-fold astigmatism is improved over that which can be achieved from analysis of Ronchigrams recorded from amorphous films. This technique can also be applied to aberration corrected STEM imaging of any hexagonal two-dimensional material.

© 2017 Elsevier B.V. All rights reserved.

1. Introduction

Aberration correctors in a modern Scanning Transmission Electron Microscopes (STEM) consist of combinations of multiple elements, deflectors and in some optical configurations round lenses [1–4]. The relationships between the strength of the various optical elements in the corrector and the aberrations in the STEM probe are complex and interconnected and in order to optimize the size and shape of the STEM probe for imaging and analysis [5] an accurate automated alignment system is required to measure and compensate residual aberrations in the STEM probe-forming optics.

A common method for measurement of the aberrations in a STEM probe involves measurement of deformations in pairs of over and underfocus images of nm sized metal particles supported on a carbon film by deconvolution probe shapes using a Gaussian focus image [6]. Alternatively, the Ronchigram can be used to calculate the aberrations from suitably conditioned measurements of beam induced image shifts [7], contrast transfer functions [8], segmentation of Ronchigrams of amorphous films [9] or a crystalline lattice

[10–13]. Finally, datasets used for electron ptychography can also provide direct measurements of probe forming aberrations [14].

As previously reported, auto-correlation functions calculated from defined areas of the Ronchigram recorded from a thin amorphous film [9] can be used to analyse the second-order derivative of the wave aberration function from which aberrations for the probe-forming system can be calculated. Previous reports [10–12] have also described methods for aberration measurement using local Ronchigrams calculated from a crystalline sample from measurements of the magnifications in local angular areas. This latter method is both fast and accurate since only a single Ronchigram is required and the local magnification is readily determined from high contrast features arising from the periodic lattice.

However, although the computational analysis of a single Ronchigram of a crystalline sample is fast it requires orientation of a sample to a specific, known zone axis which takes time and requires significant manual skill. A more fundamental problem with these methods is that a finite, generally unknown specimen thickness leads to inaccuracies in defocus measurement.

In this work auto-correlation patterns calculated from segmented areas of a Ronchigram of monolayer graphene have been used to determine the local magnification and hence the aberrations in the probe forming system. The use of a thin two-dimensional material, in this case graphene, overcomes both the practical difficulties of zone axis alignment and the fundamental

* Corresponding author at: Department of Materials, University of Oxford, Parks Road, Oxford OX1 3PH, UK.

E-mail addresses: hidetaka.sawada@jeoluk.com, hide.sawada@materials.ox.ac.uk (H. Sawada).

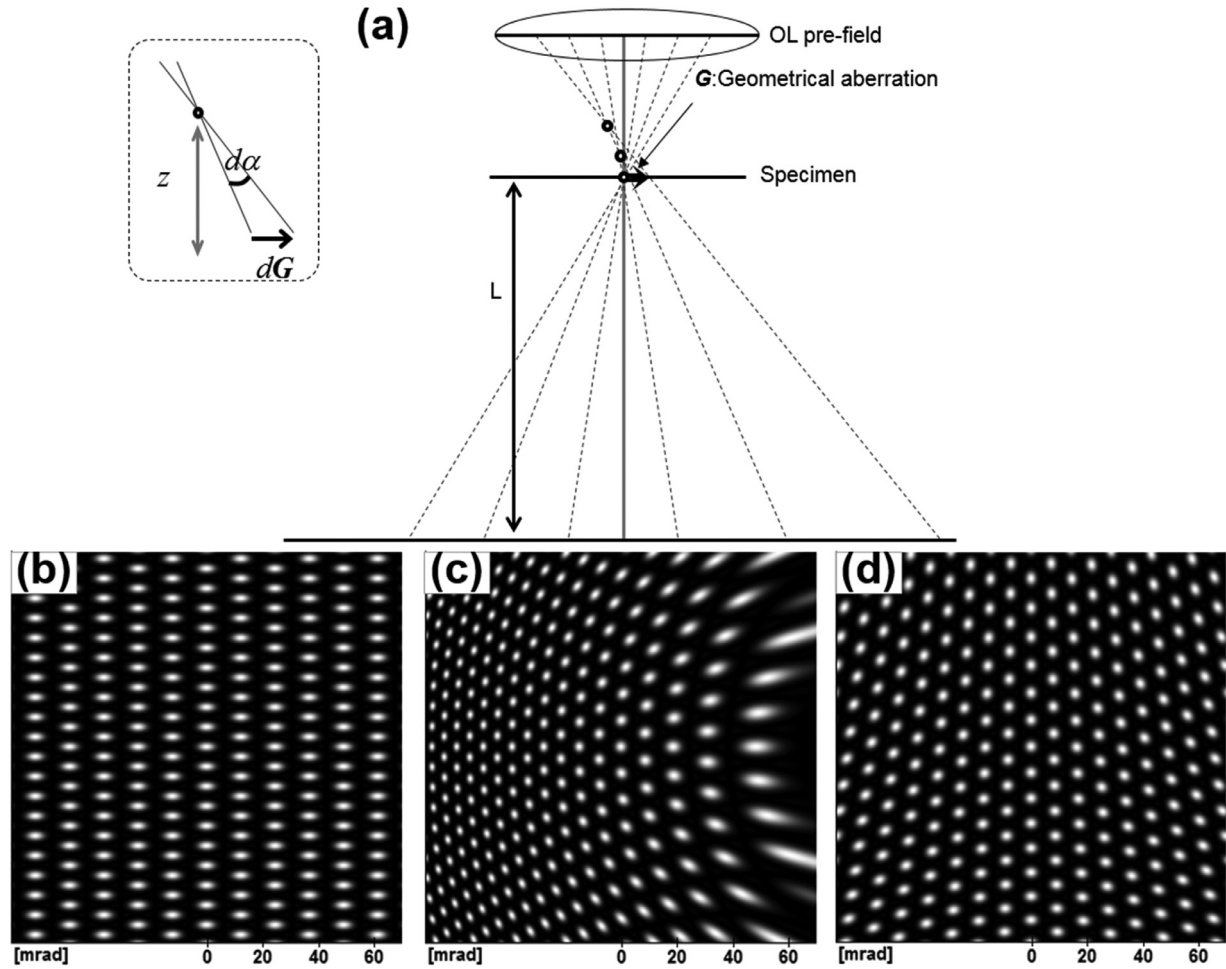


Fig. 1. (a) Schematic ray diagram for the formation of a Ronchigram in the presence of geometric aberrations. Calculated Ronchigrams with (b) two-fold astigmatism, $a_2 = 10$ nm and $\theta_{a2} = 0^\circ$, (c) axial coma, $p_3 = 200$ nm and $\theta_{p3} = 0^\circ$ and (d) three-fold astigmatism, $a_3 = 30$ nm and $\theta_{a3} = 30^\circ$. Defocus, $\sigma_2 = -30$ nm in (b)–(d). The simulated specimen in all cases is a simple hexagonal lattice with a lattice constant of 0.246 nm.

limitations associated with thick specimens. Furthermore, the features in an angular area of a two-dimensional lattice are robust to beam or specimen tilt compared to those in thicker crystalline specimens as the reciprocal lattice of a thin two-dimensional structure is extended along the electron trajectory in the z direction. For practical implementation we note that high quality graphene TEM samples are now commercially available [15].

2. Theory

A convergent beam impinging on a sample plane produces a Ronchigram in the far field [16]. This Ronchigram can be considered as the pattern formed from an electron probe focused at or near the specimen plane, projected to a far plane (determined by the camera length of the projector optics). When the probe-forming system contains geometrical aberrations, the electron beam does not converge to a single crossover, but instead, the crossover position depends on local angular position, as shown schematically in Fig. 1(a). As a consequence, axial aberrations in the probe-forming lens system are visible in the Ronchigram [17,18].

Fig. 1(b–d) shows calculated Ronchigrams of a geometric hexagonal lattice in the presence of various low order geometrical aberrations. In all cases, the hexagonal symmetry of the simulated Ronchigram is distorted by the presence of geometric aberrations in the probe-forming lens.

The lattice spacing within a local angular area of a Ronchigram, D , is described by [7,18];

$$D = \frac{L \cdot d}{z} = \frac{L \cdot d}{\left(\frac{\partial G_\alpha}{\partial \alpha}\right)} = M \cdot d. \quad (1)$$

where L is the camera length, d the lattice spacing of the specimen, z the distance between the probe crossover and the specimen plane and with M the local magnification. For an aberrated beam, z is defined by the differential of the geometrical aberration (G_α) with respect to the convergence semi-angle (α).

Eq. (1) shows that the value of the local magnification varies across the Ronchigram, leading to an overall distortion described by the product of L and the differential of the geometric aberration, $M = L \cdot \left(\frac{\partial G_\alpha}{\partial \alpha}\right)^{-1}$ [7,18].

Distortions in a segment of a Ronchigram (Fig. 2) are characterized by the geometric aberration function (Table A1) as;

$$\mathbf{G}(\omega_0 + \Delta\omega) \approx \Delta\mathbf{G}|_{\omega_0} \cdot \Delta\omega = (\Delta G_u, \Delta G_v)|_{\omega_0} \quad (2)$$

where

$$\Delta G_u|_{\omega_0} = A \cdot \Delta\omega_u + B \cdot \Delta\omega_v \quad (3)$$

$$\Delta G_v|_{\omega_0} = B \cdot \Delta\omega_u + C \cdot \Delta\omega_v \quad (4)$$

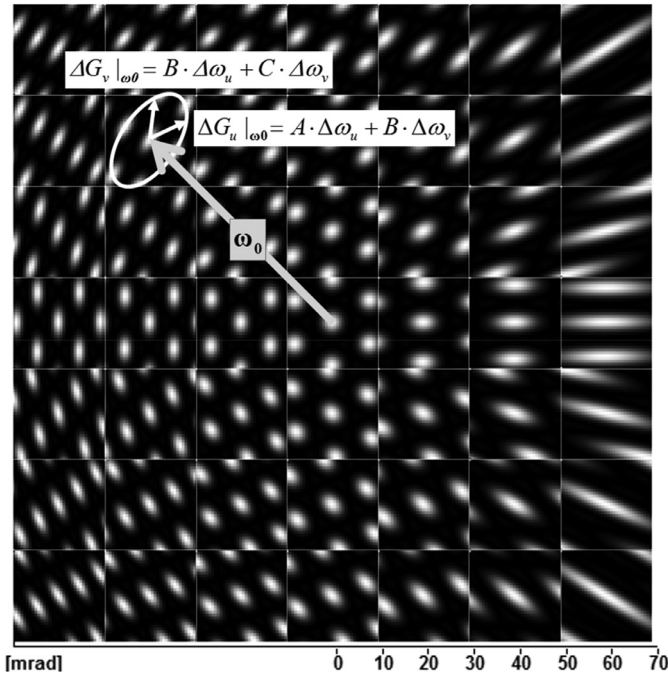


Fig. 2. Simulated segmented Ronchigram illustrating the definition of local geometric aberrations. Each of the 7×7 segments in the simulation were separately calculated using Eq. (2) with values of $P3 = 200$ nm ($\theta_{P3} = 0^\circ$) and $O2 = -30$ nm, corresponding to the aberrations used to calculate Fig. 1(c).

and

$$A = \frac{\partial G_u}{\partial \omega_u} \Big|_{\omega_0}, \quad B = \frac{\partial G_u}{\partial \omega_v} \Big|_{\omega_0}, \quad C = \frac{\partial G_v}{\partial \omega_v} \Big|_{\omega_0} \quad (5)$$

In Eq. (2) ω_0 is a vector defining the position of centre of a segment in the Ronchigram with respect to the pattern centre and where $(\Delta\omega_u, \Delta\omega_v)$ are small distances along directions (u, v) , that define the reciprocal space co-ordinates the Ronchigram [4].

The factors A , B , and C in Eq. (5) and are listed in Table A2 for all aberration coefficients up to fifth order.

3. Experimental

Aberration coefficients were measured from data recorded using a JEM-ARM300F equipped with STEM and TEM ETA spherical aberration correctors [3]. Ronchigrams were recorded at an accelerating voltage of 80 kV from a monolayer graphene sample on a Gatan Oneview camera with 4096×4096 pixels using a focused STEM probe (Fig. 3(a)). The Ronchigram was divided into local angular areas and the lateral magnification change in two directions for each segment was measured using the auto-correlation function (Fig. 3(b)). As a consequence of symmetry the auto-correlation function from each segment consists of six secondary peaks in a two-fold symmetric arrangement surrounding the central peak and hence only half the peaks (marked I, II, and III in Fig. 3(b)) were used for fitting. The positions of the maxima of these three peaks used were located to sub-pixel accuracy with parabolic fits and the resultant peak positions fitted to an oval function given by;

$$(A \cdot \Delta\omega_u + B \cdot \Delta\omega_v)^2 + (B \cdot \Delta\omega_u + C \cdot \Delta\omega_v)^2 = 1 \quad (6)$$

Subsequently, from these fitted parameters the aberrations for the probe forming lens were calculated from;

$$\Delta G_u \Big|_{\omega_0}^2 + \Delta G_v \Big|_{\omega_0}^2 = d^2 \cdot L^2 \cdot \{ (A \cdot \Delta\omega_u + B \cdot \Delta\omega_v)^2 + (B \cdot \Delta\omega_u + C \cdot \Delta\omega_v)^2 \} \quad (7)$$

where d is the lattice parameter of graphene and L is the camera length. Since the lattice parameter of graphene is known only one Ronchigram is required to calculate the aberration coefficients.

In pixel coordinates Eq. (7) can be re-written as;

$$\Delta G_u \Big|_{\omega_0}^2 + \Delta G_v \Big|_{\omega_0}^2 = d^2/k^2 \cdot \{ (A_{[1/pix]} \cdot \Delta\omega_u + B_{[1/pix]} \cdot \Delta\omega_v)^2 + (B_{[1/pix]} \cdot \Delta\omega_u + C_{[1/pix]} \cdot \Delta\omega_v)^2 \} \quad (8)$$

where k [rad/pixel] is the angular calibration factor calibrated using graphene diffraction as shown in Fig. 3(c).

4. Results

4.1. Defocus measurement

Fig. 4(a–j) shows experimental Ronchigrams recorded at 80 kV with a camera length of 40 cm from a monolayer graphene sample [15] with a 2X pixel binning for linear objective lens focus changes in 10 bit increments. The area without amorphous contamination or defects in monolayer graphene was selected for the measurement. For this data an area of 700×700 pixels was extracted with 1 pixel corresponding to an angular range of $66.18 \mu\text{rad}$. The Ronchigram was then segmented into 3×3 local angular areas (256×256 pixels) and auto-correlation patterns calculated from each area. The auto-correlation pattern from the central local area is shown at the lower left of each Ronchigram (Fig. 4) and the result of the oval fit to Eq. (6) showing a gradual change in size with defocus is indicated by the red line. The value of defocus measured from each Ronchigram is shown in Fig. 4(k). These measured values were fitted to a linear function with a slope of 0.75 nm/bit corresponding to the defocus increment/bit of the objective lens at 80 kV. In Fig. 4, here is a small residual two-fold astigmatism giving rise to the small oval distortion visible in (h–j).

4.2. Measurement of axial-coma and three-fold astigmatism

Fig. 5(a) shows a Ronchigram recorded at 80 kV with a camera length of 40 cm with a 2X pixel binning from monolayer graphene [15] with a focused STEM probe in which a known 2nd order axial coma was intentionally introduced. For this data an area of 650×650 pixels was extracted with 1 pixel corresponding to an angular range of $66.18 \mu\text{rad}$. The Ronchigram was then segmented into 3×3 local angular areas (256×256 pixels) and auto-correlation patterns calculated from each area. Fits to the six peaks in the auto-correlation pattern for each segment are shown in Fig. 5(b). The size of the fitted oval functions from segments extracted from the right hand side of the Ronchigram are larger than those from the left and the shape of the fitted function also changes from right to left. These effects are due to the local defocus at the right of the Ronchigram being closer to the Gaussian focus as a result of the introduced 2nd order axial-coma. Table 1 lists the aberration coefficients up to third order calculated from the oval fits shown in Fig. 5(b) including a large value of 2nd order axial coma value closely corresponding to that introduced.

Similarly Fig. 5(d) shows a Ronchigram recorded from monolayer graphene under the same conditions as in Fig. 5(a) but for which a known value of three-fold astigmatism has been deliberately introduced together with corresponding fits to the auto-correlation pattern for each segment (Fig. 5(e)). A three-fold symmetry is evident in the orientation of the 9 fitted oval functions. Table 2 lists the aberration coefficients up to third order calculated from the oval fits shown in Fig. 5(d) including a large value for three-fold astigmatism corresponding closely to that deliberately introduced. Fig. 5(c and f) shows simulated Ronchigrams using the measured values of the aberrations in Tables 1 and 2 respectively. The magnification change and deformation in the

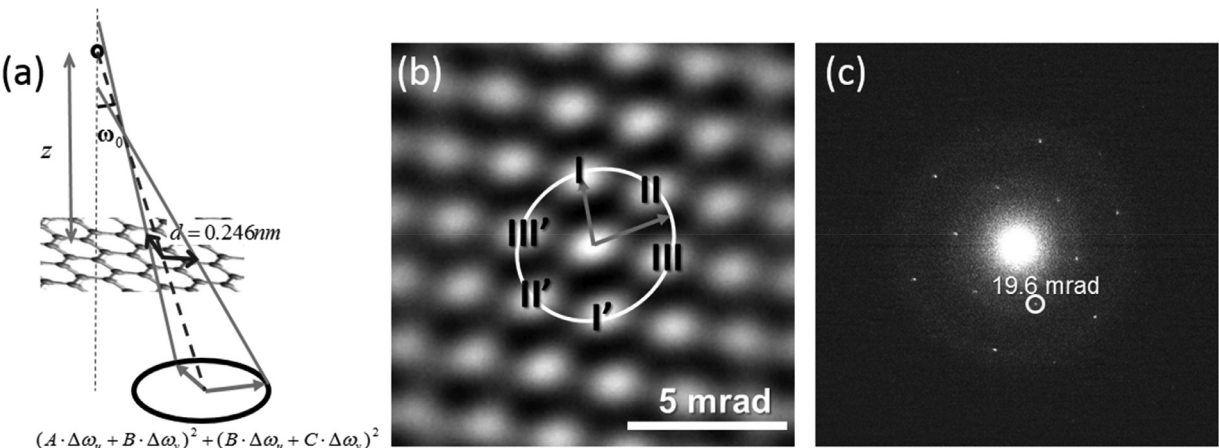


Fig. 3. (a) Schematic diagram showing the relationship between a graphene specimen and the corresponding oval shape in the Ronchigram. (b) Auto-correlation pattern calculated from a segmented area of an experimental Ronchigram calculated from a monolayer graphene specimen showing peak positions (with those generated from two-fold symmetry marked with a prime) and the oval fit to three peaks. (c) Diffraction pattern recorded from a monolayer graphene sample using parallel illumination.

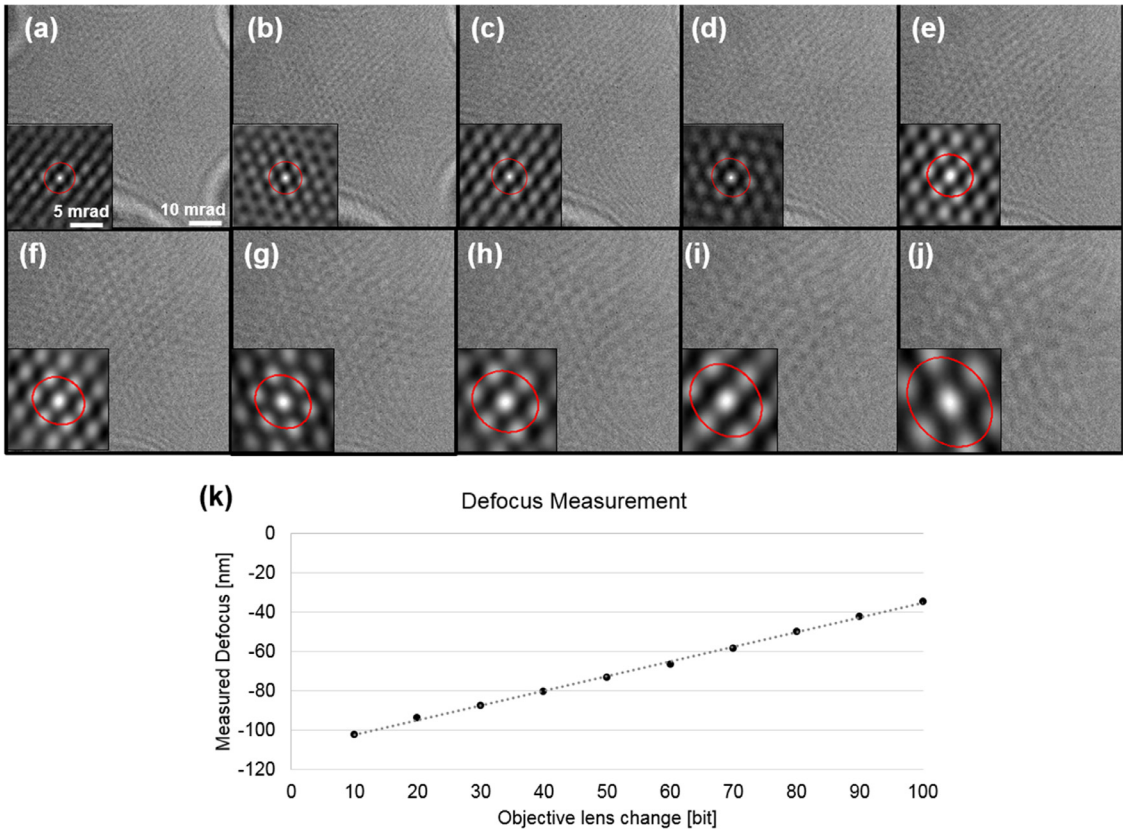


Fig. 4. (a–j) Experimental Ronchigrams (700 × 700 pixels) recorded from monolayer graphene for known changes in objective lens excitation (10 bit increments). Insets show enlargements (256 × 256 pixels) of the central angular region of the full auto-correlation pattern. (k) Measured defocus calculated from (a–j) as a function of change in the objective lens excitation together with a least squares fitted linear function with a slope of 0.75.

Table 1
Measured aberration coefficients to third order of the probe forming system calculated from the measurements shown in Fig. 5(a and b). Values in brackets correspond to errors in the measurement values [9]. The error in azimuth is described by 360°/symmetry expressed as a percentage.

Aberration	Amplitude	Azimuth
O2: Defocus	−74.35 [nm] (0.36 [nm])	
A2: Two-fold stigmatism	4.01 [nm] (1.00 [nm])	60.03° (2.49%)
P3: Axial Coma	330.64 [nm] (15.54 [nm])	−13.83° (1.90%)
A3: Three-fold astigmatism	72.16 [nm] (19.00 [nm])	35.30° (4.81%)
A4: Four-fold astigmatism	0.44 [μm] (0.75 [μm])	−43.25° (32.59%)
Q4: Star aberration	3.98 [μm] (1.42 [μm])	−59.80° (7.00%)
O4: 3rd order spherical aberration	0.98 [μm] (0.80 [μm])	

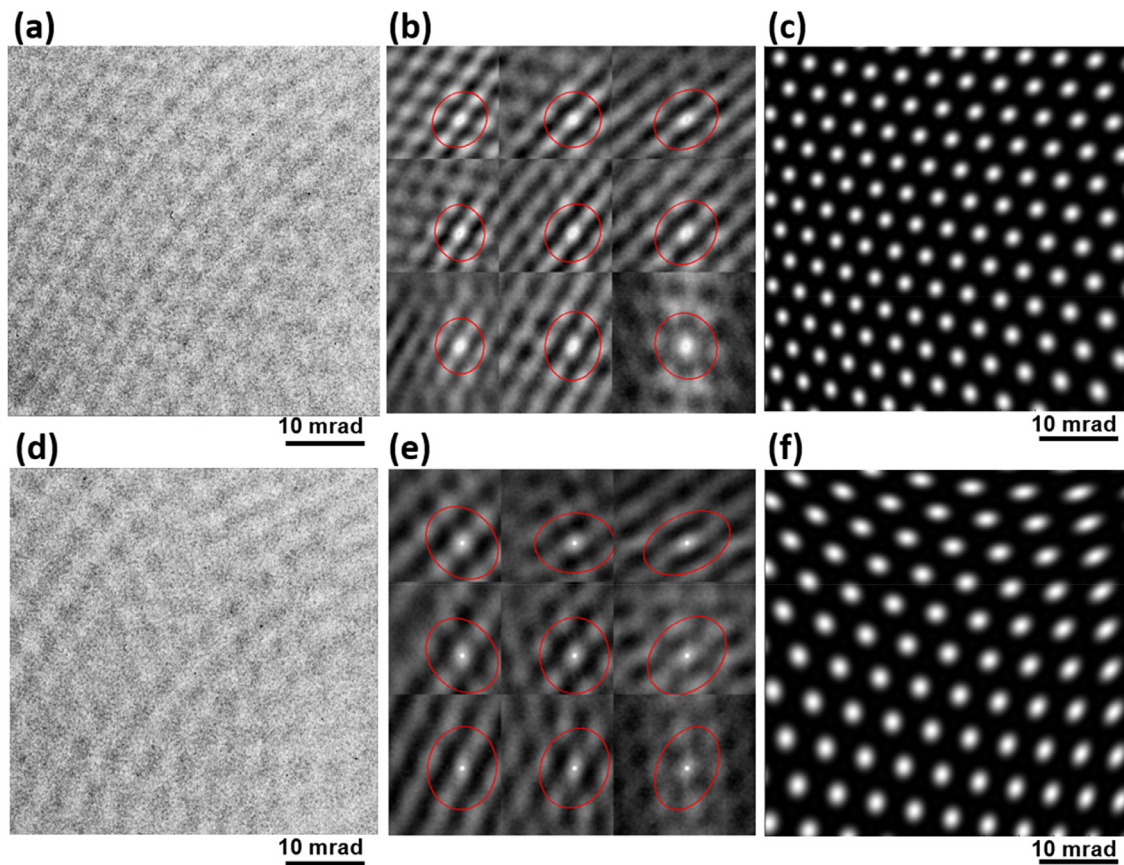


Fig. 5. (a and d) Experimental Ronchigrams (650×650 pixels) recorded from monolayer graphene with (a) 2nd order axial coma (of order 100 nm) and (d) three-fold astigmatism (of order 100 nm) intentionally introduced. (b and e) Local area auto-correlation functions (650×650 pixels) calculated from the Ronchigrams in (a) and (d) together with corresponding oval fits. (c and f) Simulated Ronchigrams for a simple hexagonal lattice with $d=0.246$ nm using the aberration coefficients measured from (b) and (e) respectively (Tables 1 and 2).

Table 2

Measured aberration coefficients to third order of the probe forming system calculated from the measurements shown in Fig. 5(d and e). Values in brackets correspond to errors in measurement values. The error in azimuth is described by $360^\circ/\text{symmetry}$ expressed as a percentage.

Aberration	Amplitude	Azimuth
O2: Defocus	-58.21 [nm] (0.77 [nm])	
A2: Two-fold stigmatism	2.08 [nm] (0.74 [nm])	59.66° (6.80%)
P3: Axial Coma	53.23 [nm] (24.24 [nm])	-116.79° (7.52%)
A3: Three-fold astigmatism	243.77 [nm] (14.07 [nm])	25.89° (1.13%)
A4: Four-fold astigmatism	3.21 [μm] (0.70 [μm])	-54.46° (4.45%)
Q4: Star aberration	4.15 [μm] (2.32 [μm])	18.66° (5.61%)
O4: 3rd order spherical aberration	-1.28 [μm] (1.10 [μm])	

simulated Ronchigrams reproduces the experimental data in Fig. 5(ad), indicating that the analysis described correctly determines these geometric aberrations in the probe-forming system to high accuracy.

4.3. Aberration measurement to 5th order

By increasing the number of auto-correlation patterns measured, higher order aberrations can also be measured using the method described. Fig. 6(a) shows a Ronchigram recorded at 80 kV with a camera length of 80 cm from a monolayer graphene sample [15] with a 1X pixel binning corresponding to an angular range up to 30 mrad with 1 pixel corresponding to $16.04 \mu\text{rad}$. Aberration coefficients up to 5th order were measured using an array

of 37 segmented areas each of 650×650 pixels (Fig. 6(b)). Values of the measured aberration coefficients up to 5th order are listed in Table 3. Fig. 6(c) shows a high-resolution ADF STEM image of a monolayer graphene sample recorded with the aberration conditions listed in Table 3 for which a small additional adjustment of defocus and two-fold astigmatism was performed after inserting the condenser aperture.

In the present method, the auto-correlation function pattern was obtained up to around 35 mrad at 80 kV, since a two dimensional lattice over this angle is not able to be visible due to a higher-order aberration of six-fold astigmatism. Due to this restriction of acquisition angle, accuracy of the measurement of the fifth order aberration is relatively inferior, although the measurement up to 4th order is rather accurate.

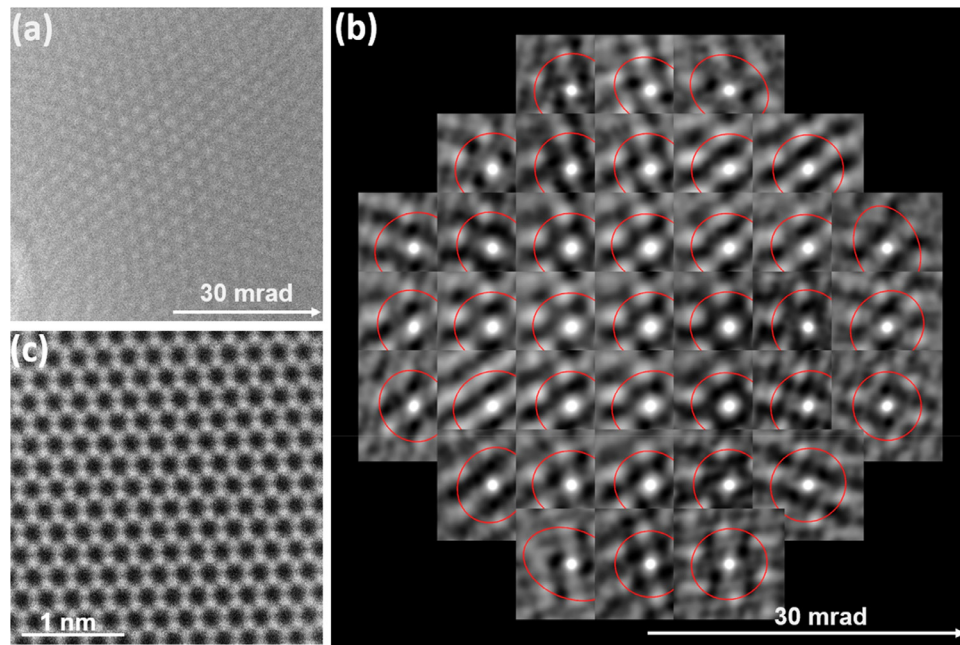


Fig. 6. (a) Experimental Ronchigram recorded ($4k \times 4k$ pixels) from monolayer graphene and the Ronchigram was shown up to 30 mrad (3740×3740 pixels). The optical axis of Ronchigram was manually adjusted at the center of the camera using deflectors in post-specimen. (b) Local area auto-correlation pattern from an array of 37 sub-areas (650×650 pixels) and fitted oval functions. (c) Low angle annular dark field (LAADF) image of monolayer graphene at 80 kV recorded with a convergence semi-angle of 25.2 mrad and beam current of 23 pA using the aberration conditions listed in Table 3. The inner and outer detection angles for the LAADF image are 39 mrad and 180 mrad respectively. Ten frames were averaged to produce the image in (c) with a dwell time of 100 μ s/pixel with 8.2 pm/pixel for each frame.

Table 3

Measured aberration coefficients to fifth order of the probe forming system calculated from the measurements shown in Fig. 6. Values in brackets correspond to errors in measurement values. The error in azimuth is described by $360^\circ/\text{symmetry}$ expressed as a percentage.

Aberration	Amplitude	Azimuth
O2: Defocus	-72.554 [nm] (0.29 [nm])	
A2: Two-fold stigmatism	1.953 [nm] (0.29 [nm])	-11.02° (2.11%)
P3: Axial Coma	49.310 [nm] (18.57 [nm])	80.40° (5.61%)
A3: Three-fold astigmatism	14.893 [nm] (10.30 [nm])	-24.56° (12.71%)
A4: Four-fold astigmatism	0.272 [μ m] (0.22 [μ m])	-29.74° (8.35%)
Q4: Star aberration	0.885 [μ m] (0.35 [μ m])	86.13° (5.37%)
O4: 3rd order spherical aberration	2.421 [μ m] (1.08 [μ m])	
P5: 4th order axial coma	84.811 [μ m] (23.75 [μ m])	-130.87° (3.15%)
R5: Three lobe aberration	25.702 [μ m] (16.12 [μ m])	9.67° (8.63%)
A5: Five-fold astigmatism	17.111 [μ m] (6.51 [μ m])	-34.70° (6.67%)
O6: 5th order Spherical aberration	-4.153 [mm] (1.11 [mm])	
A6: Six-fold astigmatism	1.077 [mm] (0.28 [mm])	-10.58° (2.92%)

5. Method precision

We have measured defoci under constant electron-optical conditions to evaluate the precision of this method for comparison with a similar analysis using an amorphous sample. The value of the defocus was set at -65 nm and 100 Ronchigrams were recorded over a 7.5 min period on a Gatan OneView camera with 1X pixel binning (4096×4096 pixel field of view) at a camera length of 80 cm. An area of 1530×1530 pixels was selected with 1 pixel corresponding to 16.04μ rad. Subsequently, $16 \times 670 \times 670$ pixel auto-correlation patterns in a 4×4 array were calculated from within the experimental Ronchigram. The measured values of defoci are shown in Fig. 7(a). The linear term in the data of Fig. 7(a) gives a defocus [nm] = -64.36 [nm] + 0.057 [nm/min] $\times t$ [min] which gives a specimen drift of 57 pm/min in the z direction for the conditions used. To estimate the precision of the measurement, this linear term was subtracted from the data, as shown in Fig. 7(b) giving a standard deviation in the measurements of 0.2408 nm. In

order to compare the precision of this method to that previously reported using the segmented Ronchigram auto-correlation matrix (SRAM) [9] data using an amorphous specimen was also acquired. For this latter dataset 100 Ronchigrams were also acquired at a camera length 40 cm for each defocus measurement using a 9×9 matrix of two images at defoci of +70 nm and -70 nm. The linear specimen term was also subtracted from the raw data and the resultant measurements are shown in Fig. 7(c) as a function of the number of measurements. The standard deviation calculated from Fig. 7(c) is 1.374 nm. Hence the precision of the measurement of defocus from the new method described using a two dimensional material is 5.7X better than the SRAM method using an amorphous film.

Fig. 8 shows two-fold astigmatism measurements calculated from both the segmented Ronchigram using monolayer graphene and the SRAM method using an amorphous film. The mean value has been subtracted from both data sets to enable clear visualization of the precision in a single measurement. The standard deviation

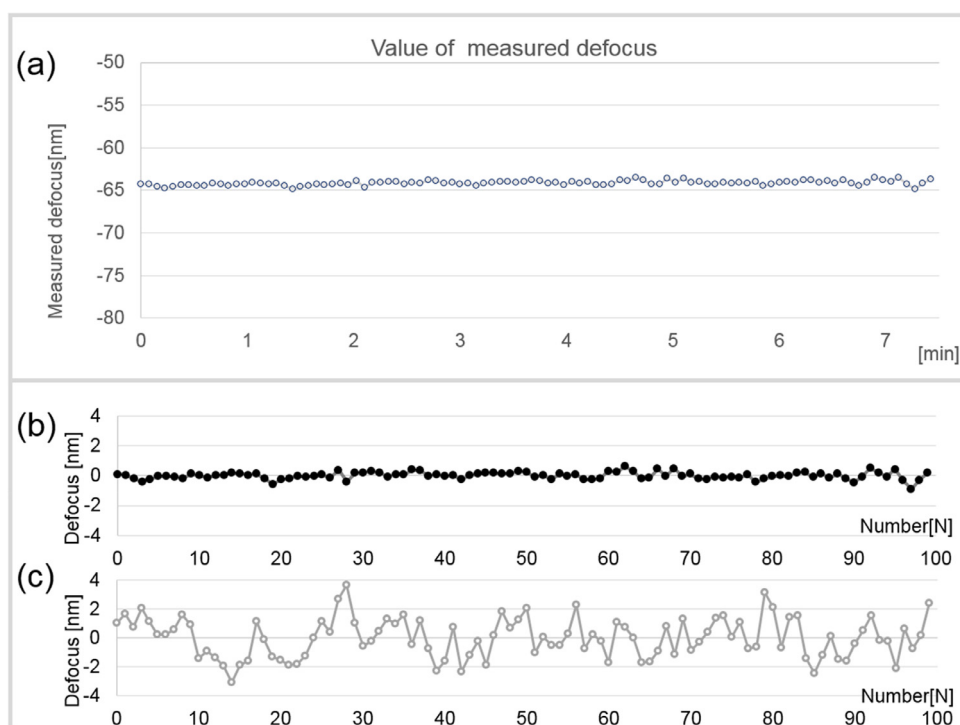


Fig. 7. (a) Measurement of defocus as a function of time (minutes) for a constant objective defocus for 100 measurements using segmentation of Ronchigrams recorded from monolayer graphene. (b) Measurement of defocus as a function of repeated measurement after subtracting the linear specimen drift term of $0.0569 \text{ [nm/min]} \times t \text{ [min]}$ from (a). (c) Measurement of defocus as a function of repeated measurement calculated from the SRAM using an amorphous film [9] after subtracting the linear specimen drift term of $0.519 \text{ [nm/min]} \times t \text{ [min]}$.

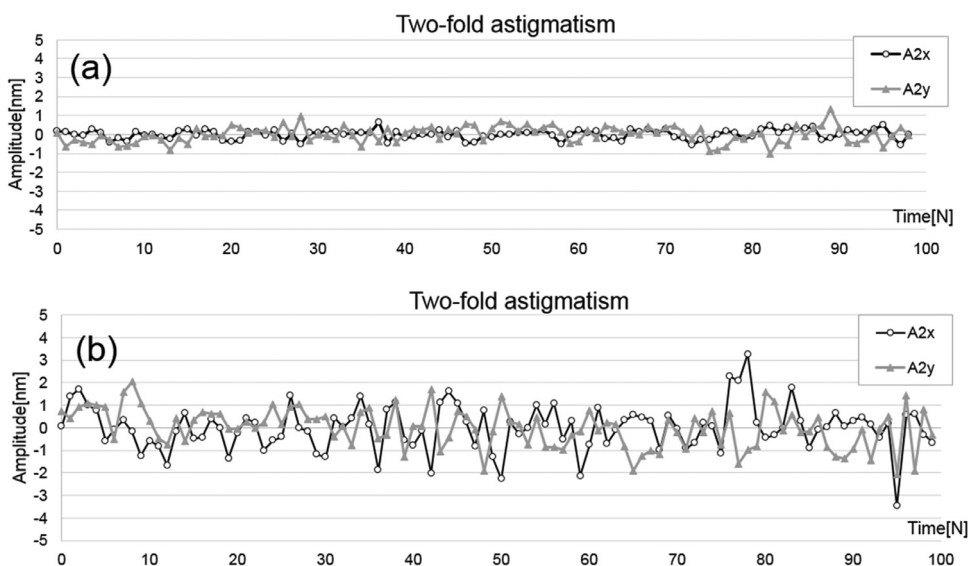


Fig. 8. (a) Deviation from the mean two-fold astigmatism in the x ($A2x$) and y ($A2y$) directions respectively measured using segmentation of the Ronchigram from monolayer graphene. Standard deviations of the measurements in $A2x$ and $A2y$ are 0.25 nm and 0.43 nm respectively. (b) Deviation from the mean two-fold astigmatism measurement measured from the SRAM [9] using an amorphous film. The standard deviation of the measurements in $A2x$ and $A2y$ are 1.00 nm and 0.88 nm respectively.

tion of the two-fold astigmatism measurement from the segmentation of the Ronchigram using monolayer graphene ($A2x = 0.25 \text{ nm}$, $A2y = 0.43 \text{ nm}$) is less than half that as measured using an amorphous film ($A2x = 1.00 \text{ nm}$, $A2y = 0.88 \text{ nm}$).

6. Aberration measurement using MoS_2

This method described can easily be adapted to use other monolayer two-dimensional materials, such as MoS_2 by simply

changing the two-dimensional lattice parameter used for the analysis. To illustrate this a monolayer MoS_2 sample (2 dimensional lattice coefficient 0.27 nm) grown by chemical vapour deposition (CVD) [19] was used to measure the geometric aberration coefficients up to 3rd order in the probe-forming system. A 37 array of (600×600 pixel) segmented sub-areas from a field of view, as shown in Fig. 9(a and b), was used in the calculations. Measured aberration coefficients are listed in Table 4. Fig. 9(c) shows a high-resolution ADF STEM image of a monolayer MoS_2 at 80 kV .

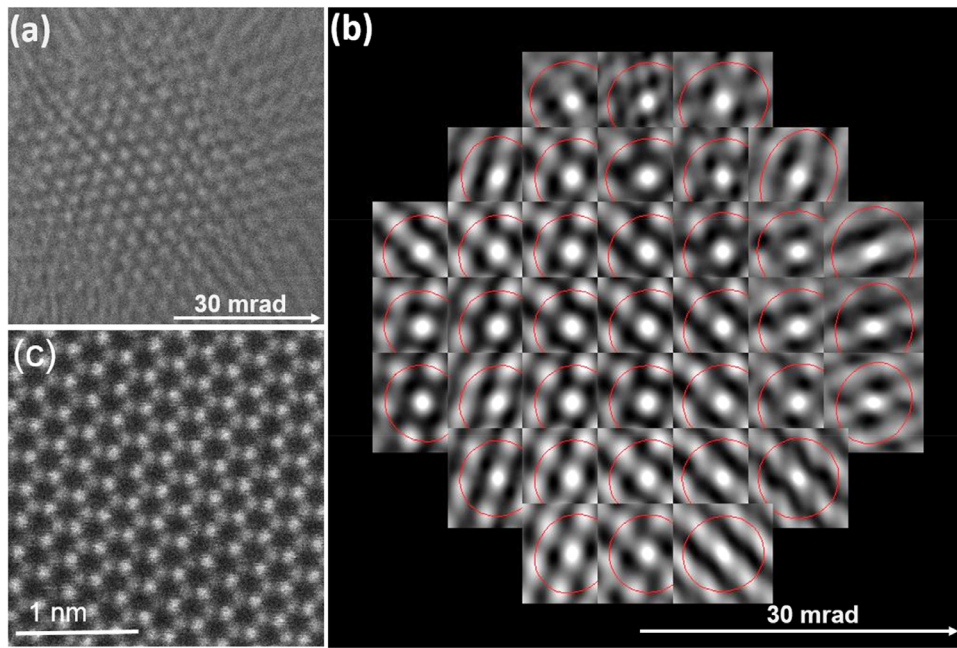


Fig. 9. (a) Experimental Ronchigram recorded from monolayer MoS₂ with a STEM probe at a camera length of 80 cm at 80 kV. Auto-correlation patterns were calculated from the area indicated by the white square. (b) Local area auto-correlation patterns from an array of 37 sub-areas (600 × 600 pixels) and corresponding oval fits. (c) LAADF image of monolayer MoS₂ recorded at 80 kV using the aberration conditions listed in Table A3. The STEM image acquisition parameters are same as those in Fig. 6(c). The sampling time is 10 μs pm/pixel for a sampling of 7.1 pm/pixel.

Table 4

Measured aberration coefficients to fifth order of the probe forming system calculated from the measurements shown in Fig. 9. Values in brackets correspond to errors in measurement values. The error in azimuth is described by 360°/symmetry expressed as a percentage.

Aberration	Amplitude	Azimuth
O2: Defocus	−72.027 [nm] (0.24 [nm])	
A2: Two-fold stigmatism	1.089 [nm] (0.22 [nm])	24.52° (2.18%)
P3: Axial Coma	112.117 [nm] (11.42 [nm])	− 8.92° (1.90%)
A3: Three-fold astigmatism	19.433 [nm] (8.40 [nm])	−52.53° (6.43%)
A4: Four-fold astigmatism	1.179 [μm] (0.12 [μm])	−39.28° (1.96%)
Q4: Star aberration	1.526 [μm] (0.18 [μm])	71.11° (2.98%)
O4: 3rd order spherical aberration	0.650 [μm] (0.89 [μm])	
P5: 4th order axial coma	99.396 [μm] (15.81 [μm])	137.63° (2.34%)
R5: Three lobe aberration	55.617 [μm] (13.37 [μm])	27.15° (2.59%)
A5: Five-fold astigmatism	36.462 [μm] (4.57 [μm])	−31.84° (2.22%)
O6: 5th order Spherical aberration	0.515 [mm] (0.95 [mm])	
A6: Six-fold astigmatism	1.285 [mm] (0.20 [mm])	−3.14° (2.14%)

7. Measurement of chromatic aberration

As the presented method can measure the absolute value of the defocus in the probe-forming system to high precision, it can be applied to accurate measurement of chromatic aberration. A defocus spread df_{Cc} due to chromatic aberration with an energy deviation of dE is defined as $df = -Cc \cdot dE/E$.

A coefficient of chromatic aberration can be defined as,

$$Cc = -E \frac{df_{Cc}}{dE} \quad (9)$$

where E is the accelerating voltage.

The chromatic aberration coefficient after relativistic correction is given by $Cc = Cc^*(1 + 2\varepsilon E)/(1 + \varepsilon E)$, where $\varepsilon = 0.9785 \times 10^{-6}$ [6] and Cc^* is a nonrelativistic chromatic aberration coefficient. Cc can be derived from the slope of the defocus change with energy

shift as given by Eq. (9). Fig. 10 shows Ronchigrams and corresponding auto-correlation functions recorded with increasing accelerating voltage from 80 kV in increments, $dE = 1$ eV. The measured defocus value as a function of energy shift is shown in Fig. 10 giving a value of $Cc^* = 0.952$ mm and $Cc = 1.02$ mm at 80 kV for the probe-forming system.

8. Conclusions

We have described a method for accurate measurement of the axial geometric aberrations in a probe forming system up to 5th order using analysis of a single Ronchigram measured from monolayer two-dimensional materials. Auto-correlation functions calculated from segmented angular areas have been used to estimate local distance and distortion in the two-dimensional lattice parameter measured from the Ronchigram. Substantially lower standard deviations in the measurement of defoci and two-fold astigmatism

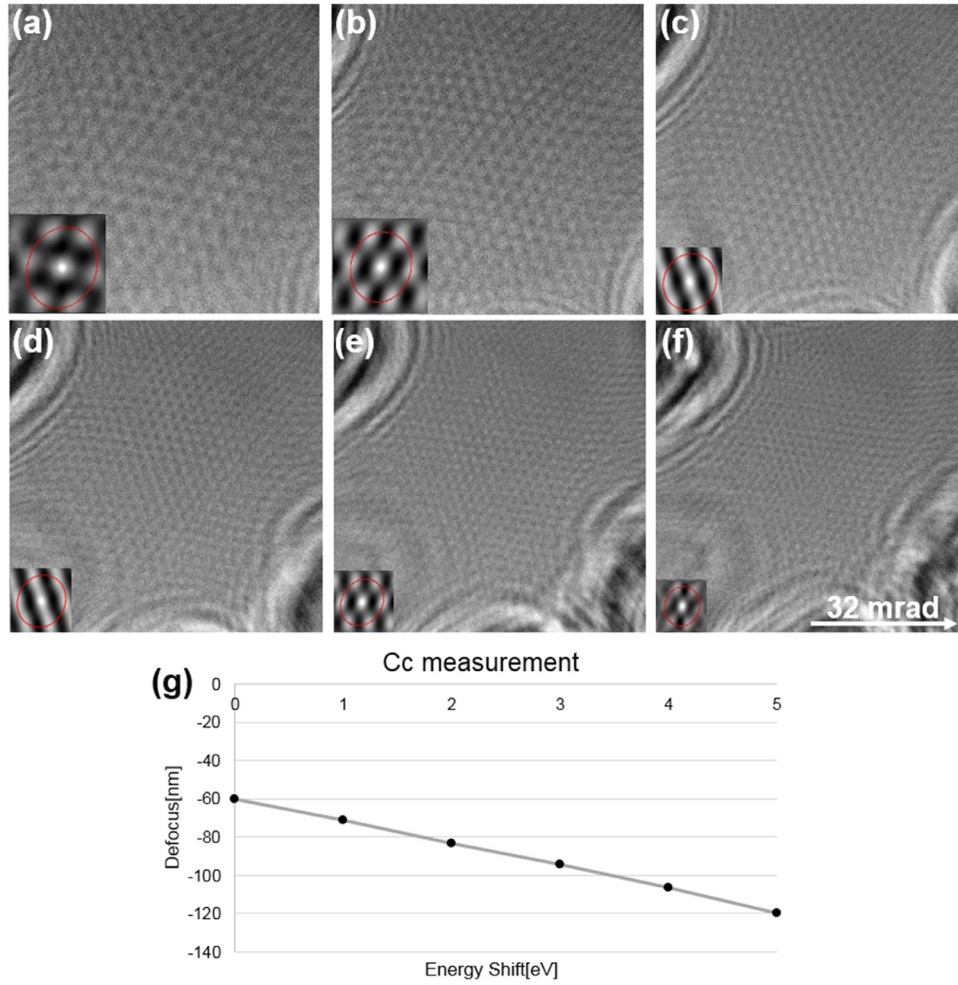


Fig. 10. (a–f) Experimental Ronchigrams recorded from monolayer graphene with varying accelerating voltage. Insets show auto-correlation patterns used to measure defocus. (a) $dE = 0$ eV, (b) $dE = +1$ eV, (c) $dE = +2$ eV, (d) $dE = +3$ eV, (e) $dE = +4$ eV and (f) $dE = +5$ eV. Ronchigrams were recorded at a camera length of 80 cm up to 32 mrad. (g) Value of defoci from Fig. 10 (a–f) as a function of energy shift. The slope is calculated to be -11.9 [nm/eV] at 80 kV.

have been demonstrated compared to equivalent data recorded from an amorphous specimen measured using the previously reported SRAM. The validity of this method has also been demonstrated for measurements of higher order aberration coefficients and has been further applied to measure the coefficient of chromatic aberration for the probe-forming system.

Appendix 1. Geometric aberrations

The complex geometric aberration coefficients are listed in Table A1. The complex angle $\omega = \alpha \exp(i\theta) = \omega_u + i\omega_v = \lambda(u + iv)$ is defined by a convergence angle α , with an azimuth θ , where λ is the wavelength of the incident electrons.

Table A1, Table A2.

Table A1

Definition of geometric aberrations and aberration coefficients. Definition of positive direction of the azimuth sign is anticlockwise on Ronchigram pattern.

Axial aberration	Notation	Coefficient	Geometric aberration
Defocus	O_2	o_2	$O_2\omega$
Two-fold astigmatism	A_2	$a_2 \exp(2i\theta_{a2})$	$A_2\tilde{\omega}$
Axial coma	P_3	$p_3 \exp(i\theta_{p3})$	$1/3 \cdot \overline{P_3}\tilde{\omega}^2 + 2/3 \cdot P_3\tilde{\omega}\omega$
Three-fold astigmatism	A_3	$a_3 \exp(3i\theta_{a3})$	$A_3\tilde{\omega}^2$
Third order spherical aberration	O_4	o_4	$O_4\tilde{\omega}\omega^2$
Star aberration	Q_4	$q_4 \exp(2i\theta_{q4})$	$1/4 \cdot \overline{Q_4}\tilde{\omega}^3 + 3/4 \cdot Q_4\tilde{\omega}^2\omega$
Four-fold astigmatism	A_4	$a_4 \exp(4i\theta_{a4})$	$A_4\tilde{\omega}^3$
Fourth order axial coma	P_5	$p_5 \exp(i\theta_{p5})$	$2/5 \cdot \overline{P_5}\tilde{\omega}\omega^3 + 3/5 \cdot P_5\tilde{\omega}^2\omega^2$
Three lobe aberration	R_5	$r_5 \exp(3i\theta_{r5})$	$1/5 \cdot \overline{R_5}\tilde{\omega}^4 + 4/5 \cdot R_5\tilde{\omega}^3\omega$
Five-fold astigmatism	A_5	$a_5 \exp(5i\theta_{a5})$	$A_5\tilde{\omega}^4$
Fifth order spherical aberration	O_6	o_6	$O_6\tilde{\omega}^2\omega^3$
Six-fold astigmatism	A_6	$a_6 \exp(6i\theta_{a6})$	$A_6\tilde{\omega}^5$

Table A2
Factors A, B, and C [9].

	A	B	C
O₂	o_2	0	o_2
A₂	$a_2 \cos 2(\theta_{a2})$	$a_2 \sin 2(\theta_{a2})$	$-a_2 \cos 2(\theta_{a2})$
P₃	$4/3 p_3 \alpha \cos(\theta - \theta_{p3})$ $+2/3 p_3 \alpha \cos(\theta + \theta_{p3})$	$2/3 \cdot p_3 \alpha \sin(\theta + \theta_{p3})$	$4/3 p_3 \alpha \cos(\theta - \theta_{p3})$ $-2/3 p_3 \alpha \cos(\theta + \theta_{p3})$
A₃	$2a_3 \alpha \cos(\theta - 3\theta_{a3})$	$-2a_3 \alpha \sin(\theta - 3\theta_{a3})$	$-2a_3 \alpha \cos(\theta - 3\theta_{a3})$
O₄	$2o_4 \alpha^2 + o_4 \alpha^2 \cos 2\theta$	$o_4 \alpha^2 \sin 2\theta$	$2o_4 \alpha^2 - o_4 \alpha^2 \cos 2\theta$
Q₄	$3/2 \cdot q_4 \alpha^2 \cos(\theta_{q4} - 2\theta) + 3/2 \cdot q_4 \alpha^2$	0	$3/2 \cdot q_4 \alpha^2 \cos(\theta_{q4} - 2\theta) - 3/2 \cdot q_4 \alpha^2$
A₄	$3a_4 \alpha^2 \cos(2\theta - 4\theta_{a4})$ $12/5 p_5 \alpha^3 \cos(\theta - \theta_{p5})$	$-3a_4 \alpha^2 \sin(2\theta - 4\theta_{a4})$ $6/5 p_5 \alpha^3 \sin(\theta + \theta_{p5})$	$-3a_4 \alpha^2 \cos(2\theta - 4\theta_{a4})$ $12/5 p_5 \alpha^3 \cos(\theta - \theta_{p5})$
P₅	$+6/5 p_5 \alpha^3 \cos(\theta + \theta_{p5})$ $+2/5 p_5 \alpha^3 \cos(3\theta - \theta_{p5})$	$+2/5 p_5 \alpha^3 \sin(3\theta - \theta_{p5})$	$-6/5 p_5 \alpha^3 \cos(\theta + \theta_{p5})$ $-2/5 p_5 \alpha^3 \cos(3\theta - \theta_{p5})$
R₅	$8/5 r_5 \alpha^3 \cos(3\theta - \theta_{r5})$ $+12/5 r_5 \alpha^3 \cos(\theta - \theta_{r5})$	$-12/5 r_5 \alpha^3 \sin(\theta - \theta_{r5})$	$8/5 r_5 \alpha^3 \cos(3\theta - \theta_{r5})$ $-12/5 r_5 \alpha^3 \cos(\theta - \theta_{r5})$
A₅	$4a_5 \alpha^3 \cos(3\theta - 5\theta_{a5})$	$-4a_5 \alpha^3 \sin(3\theta - 5\theta_{a5})$	$-4a_5 \alpha^3 \cos(3\theta - 5\theta_{a5})$
O₆	$3o_6 \alpha^4 + 2\alpha^4 o_6 \cos 2\theta$	$2\alpha^4 o_6 \sin 2\theta$	$3o_6 \alpha^4 - 2\alpha^4 o_6 \cos 2\theta$
A₆	$5a_6 \alpha^4 \cos(4\theta - 6\theta_{a6})$	$-5a_6 \alpha^4 \sin(4\theta - 6\theta_{a6})$	$-5a_6 \alpha^4 \cos(4\theta - 6\theta_{a6})$

References

- [1] M. Haider, S. Uhlemann, E. Schwan, H. Rose, B. Kabius, K. Urban, Electron microscopy image enhanced, *Nature* 392 (1998) 768.
- [2] O.L. Krivanek, M.F. Chisholm, V. Nicolosi, T.J. Pennycook, G.J. Corbin, N. Dellby, M.F. Murfitt, C.S. Own, Z.S. Szilagy, M.P. Oxley, S.T. Pantelides, S.J. Pennycook, Atom-by-atom structural and chemical analysis by annular dark-field electron microscopy, *Nature* 464 (2010) 571.
- [3] F. Hosokawa, H. Sawada, Y. Kondo, K. Takayanagi, K. Suenaga, Development of Cs and Cc correctors for transmission electron microscopy, *Microscopy* 62 (2013) 23.
- [4] H. Sawada, T. Sasaki, F. Hosokawa, S. Yuasa, M. Terao, M. Kawazoe, T. Nakamichi, T. Kaneyama, Y. Kondo, K. Kimoto, K. Suenaga, Correction of higher order geometrical aberration by triple 3-fold astigmatism field, *J. Electron Microsc.* 58 (2009) 341.
- [5] M. Watanabe, in: S.J. Pennycook, P.D. Nellist (Eds.), Chapter 7 in *Scanning Transmission Electron Microscopy: Imaging and Analysis*, Springer, NY, 2011, p. 291.
- [6] M. Haider, S. Uhlemann, J. Zach, Upper limits for the residual aberration of a high-resolution aberration-corrected STEM, *Ultramicroscopy* 81 (2000) 163.
- [7] N. Dellby, O.L. Krivanek, P.D. Nellist, P.E. Batson, A.R. Lupini, Towards sub-Ångstrom electron beams, *J. Electron Microsc.* 50 (2001) 177.
- [8] A.R. Lupini, P. Wang, P.D. Nellist, A.I. Kirkland, S.J. Pennycook, Aberration measurement using the Ronchigram contrast transfer function, *Ultramicroscopy* 110 (2010) 891.
- [9] H. Sawada, T. Sannomiya, F. Hosokawa, T. Nakamichi, T. Kaneyama, T. Tomita, Y. Kondo, T. Tanaka, Y. Oshima, Y. Tanishiro, K. Takayanagi, Measurement method of aberration from Ronchigram by autocorrelation function, *Ultramicroscopy* 108 (2008) 1467.
- [10] A.R. Lupini, S.J. Pennycook, Rapid auto tuning for crystalline specimens from an inline hologram, *J. Electron Microsc.* 57 (2008) 195.
- [11] T. Yamazaki, Y. Kotaka, Y. Kikuchi, K. Watanabe, Precise measurement of third-order spherical aberration using low-order zone-axis Ronchigrams, *Ultramicroscopy* 106 (2006) 153.
- [12] K. Kuramochi, T. Yamazaki, Y. Kotaka, Y. Kikuchi, I. Hashimoto, K. Watanabe, Measurement of twofold astigmatism of probe-forming lens using low-order zone-axis ronchigram, *Ultramicroscopy* 108 (2008) 339.
- [13] Q.M. Ramasse, A.L. Bleloch, Diagnosis of aberrations from crystalline samples in scanning transmission electron microscopy, *Ultramicroscopy* 106 (2005) 37.
- [14] H. Yang, R.N. Rutte, L. Jones, M. Simson, R. Sagawa, H. Ryll, M. Huth, T.J. Pennycook, H. Soltan, Y. Kondo, B.D. Davis, P.D. Nellist, Simultaneous atomic-resolution electron ptychography and Z-contrast imaging of light and heavy elements in complex nanostructures, *Nat. Commun.* 7 (2016) 12532.
- [15] Graphene samples from Graphenea Inc. (<https://www.graphenea.com>).
- [16] V. Ronchi, Forty Years of History of a Grating Interferometer, *Appl. Opt.* 3 (1964) 437.
- [17] J.M. Cowley, Coherent interference in convergent beam electron diffraction and shadow imaging, *Ultramicroscopy* 4 (1979) 435.
- [18] J.M. Cowley, Electron diffraction Phenomena Observed with a high resolution STEM instrument, *J. Electron Microsc.* 3 (1986) 25.
- [19] S. Wang, M. Pacios, H. Bhaskaran, J.H. Warner, Substrate control for large area continuous films of monolayer MoS₂ by atmospheric pressure chemical vapor deposition, *Nanotechnology* 27 (2016) 85604.